



ORIGINAL RESEARCH ARTICLE

Metallurgical and Corrosion Characterization of Austenitic Stainless Steel Welds during Post Weld Heat Treatment

Liamine Kaba, Ahmed Kellai, Said Dehimi, Sami Kahla, Zoheir Boutaghou, and Tarek Bendris

Submitted: 21 April 2024 / Revised: 9 July 2024 / Accepted: 17 July 2024

In this study, the effects of post weld heat treatment (PWHT) on the microstructure evolution, mechanical properties and corrosion resistance of 304 austenitic stainless steel (ASS) welds generated via the gas tungsten arc welded (GTAW) process were investigated. Weldments were subjected to PWHT at 650, 850 and 1050 °C for 1 h, followed by water quenching. Optical and scanning electron microscopy revealed equiaxed austenite grains (γ) limited by grain boundaries in the microstructure of the base metal (BM). A minor content of delta ferrite (δ) was observed at the grain boundaries, accompanied by twin crystals distributed within the austenitic matrix. Subjecting the ASS weld to PWHT at 650 °C caused the microstructure to partially recrystallize. By contrast, PWHT at 850 °C induced the formation of new small γ -grains, which was attributed to recrystallization with coarser γ -grains; this effect was particularly pronounced for PWHT at 1050 °C. The microstructure of the weld zone (WZ) remained unchanged by PWHT at all temperatures, predominantly retaining a dendritic structure containing skeletal δ -ferrite. As the temperature of the heat treatment was increased, the distribution of δ -ferrite became increasingly more uniform (particularly for treatment at 650 °C), accompanied by an increase in the width of δ -ferrite dendrites. The microhardness profiles indicated a phase instability, where the Vickers microhardness of the WZ (approximately 150 ± 10 HV) was lower than that of the BM. The highest ultimate tensile strength (UTS) observed in the as-welded joint was 670.2 MPa, but the highest elongation (E) of 20.87% occurred in the sample subjected to PWHT at 650 °C. Subjecting samples in a 3.5 wt.% NaCl solution to PWHT up to 850 °C improved the corrosion resistance of the WZ. By contrast, the as-welded BM samples exhibited greater corrosion resistance than the heat-treated samples did.

Keywords austenitic stainless steel, gas tungsten arc welding, microstructure and corrosion resistance, post weld heat treatment

1. Introduction

Owing to their excellent corrosion resistance and superior mechanical performance under various service conditions, austenitic stainless steels (ASSs) have emerged as one of the most important and widely employed families of stainless steels. ASSs are specifically employed in the high-temperature sections of boiler tubing, particularly during the late stages of superheaters and reheaters. It is crucial for steel to exhibit remarkable resistance to creep rupture and oxidation in these regions. In addition, ASSs are frequently used as materials for the components of power plants (Ref 1, 2). The solidification structure of an ASS has a single-phase, face-centered cubic

(FCC) arrangement. This structure is achieved through a balance of alloying additions that stabilize the austenite phase across a broad range of temperatures, ranging from elevated to cryogenic (Ref 3-5). Typically, austenitic stainless steel with more than 12% chromium has good corrosion resistance because of the spontaneous regeneration of a chromium oxide layer on its surface. Other alloying elements, such as nickel, manganese and molybdenum, also increase resistance to localized corrosion (Ref 3-8). The addition of copper, silicon, aluminum, and nitrogen can enhance resistance to intergranular and crevice corrosion, stress-corrosion cracking (SCC), and pitting corrosion (Ref 9).

Pitting corrosion is one of the most insidious forms of localized corrosion affecting metals and is characterized by passivation (Ref 10). Compelling technical and economic requirements across various industrial applications of ASS make the welding process the ideal manufacturing method for austenitic stainless steels (Ref 11). Some welding parameters can affect the microstructure and pitting corrosion resistance of austenitic stainless steels, especially in solutions containing chloride anions commonly present in numerous natural and industrial environments (Ref 7, 10, 12). Examples of these parameters are the current, voltage, welding speed, filler metals, and shielding-gas composition (Ref 4, 13). The welding process induces diverse thermal cycles, creating two distinct zones: a weld zone (WZ) and a heat-affected zone (HAZ). This heterogeneity may result in different corrosion resistance behaviors (Ref 4). Welding of austenitic stainless steel can

Liamine Kaba, Ahmed Kellai, Said Dehimi, Sami Kahla, Zoheir Boutaghou, and Tarek Bendris, Research Center in Industrial Technologies, P.O. Box 64, 16014 Chéraga, Algiers, Algeria. Contact e-mails: kaba05liamine@gmail.com, kellai.a.a@gmail.com, saiddehimi@yahoo.fr, samikahla40@yahoo.com, z.boutaghou@crti.dz, and tarekbendris9@gmail.com.

induce detrimental secondary phases, such as σ , nitrides and carbides, along with metastable δ -ferrite in a content the range of 2 to 10% (Ref 11, 13). These phases (along with their immediate surroundings) considerably reduce the pitting resistance by providing favorable sites for corrosion initiation. This effect is particularly pronounced in corrosive environments containing chlorides (Ref 4, 14). The sigma phase (σ) reduces corrosion resistance because of the low content of molybdenum and chromium in the austenitic matrix (Ref 9, 15). The weld zone has a greater resistance to pitting corrosion than the base metal because the delta ferrite phase forms in the base metal (Ref 7, 16). The addition of nickel and molybdenum can improve corrosion resistance (Ref 8). In conclusion, the corrosion resistance of austenitic stainless steels depends on the microstructure, chemical composition and homogeneity of their passive films.

Several methods have been proposed to improve the corrosion resistance of weldments, including controlling the welding procedure and incorporating alloying elements, such as V, Nb and Ti, to eliminate carbides (Ref 17-19). Post weld heat treatment (PWHT) is also recognized as an effective method for addressing various issues, particularly under severe corrosion (Ref 8, 20-23). The substantial quantities of chromium and molybdenum in ASS 316LN increase its corrosion resistance. However, these high elemental contents also cause the austenite phase to become unstable at temperatures ranging from 650 to 900 °C, resulting in the formation of chromium-rich carbides and intermetallic phases (Ref 15). AISI 316 L welds have been found to exhibit increased susceptibility to corrosion after being subjected to a temperature of 750 °C for 24 hours. The inclusion of titanium (Ti) and niobium (Nb) in the ASS welds was found to lead to greater preservation of nickel (Ni) and a lower loss of chromium (Cr) in dendritic regions compared to weld metals that were stabilized with Nb only (Ref 24). A welded connection of AISI 316 stainless steel was subjected to PWHT through controlled heating at 400 °C for 12 minutes. This process enhanced the resilience of steel welds against stress-corrosion cracking, particularly in the presence of hostile sulfide ions (SO_4^-) (Ref 16). 304L ASS was subjected to PWHT at 500 °C for 1, 5, and 11 days, followed by exposure to classical sensitization at 650 °C for 1, 12, and 24 hours. The varying shapes of ferrite in the weld area and the degree of grain enlargement in the HAZ of the weldments under the action of different aging conditions greatly influenced the tendency of the ASS to generate carbides. The vulnerability of the ASS to sensitization and pitting corrosion was consequently impacted considerably (Ref 4). The 304 ASS was subjected to PWHT by exposure to a temperature of 650 °C for 30 and 120 minutes, followed by a normalization process. The corrosion studies revealed that welds subjected to shorter thermal aging periods had a lower degree of sensitization (DoS) than did those subjected to longer thermal aging periods, leading to a higher DoS (Ref 25). The 304 ASS joint subjected to post weld thermal aging (PWTA) at 1050 °C for 30 minutes, followed by normalization, exhibited increased resistance to corrosion in a 3.5 wt.% NaCl solution. This improved performance over that of both the post annealed and as-welded joints can be attributed to the presence of a refined grain structure and the elimination of Cr-rich carbide precipitates (Ref 26). In conclusion, welds that have undergone controlled PWHT at elevated temperatures have good corrosion resistance. Although studies have been conducted on subjecting ASS weldments to PWHT, additional investigations need to be carried out on enhancing the

mechanical properties and corrosion resistance of ASS welds. In this study, 304 ASS was welded via the GTAW process using an ER308Si filler wire. The microstructural evolution of the as-welded and PWHT (650, 850 and 1050 °C) weldments was examined via optical microscopy (OM) and scanning electron microscopy (SEM) in conjunction with energy-dispersive spectroscopy (EDS) and x-ray diffraction (XRD). The mechanical properties of the materials were evaluated via microhardness and tensile tests, whereas the corrosion behavior was assessed through potentiodynamic anodic polarization in a 3.5 wt.% NaCl solution.

2. Novelty and Application

A limited number of studies have been performed on the effects of PWHT on the corrosion resistance of welded joints in 304 austenitic stainless steel (Ref 25). In some studies (Ref 4, 15, 16, 24 and 26), the impact of PWHT at prescribed temperatures on the corrosion resistance of different ASS grades has been investigated. The novelty of our research lies in the specific welding process used, that is, GTAW with a thin-walled (3.75-mm-thick) 304 base metal and an appropriate filler metal ER308Si. We conducted PWHT at 650, 850, and 1050 °C with a one-hour holding time, followed by water quenching.

Our welds are utilized in the oil and gas industry, namely, in the equipment section intended for incinerating oil and gas waste under high-temperature and corrosive conditions. 304 ASS exhibits potential for intergranular corrosion because of the formation of chromium carbide at grain boundaries in a temperature range of 450 to 850 °C. Therefore, studies need to be performed on the corrosion behavior of heat-treated 304 ASS welds.

3. Materials and Methods

The base metal used in this investigation was 304 austenitic stainless steel in the form of a 3.75-mm-thick pipe with an outside diameter of 203.2 mm. The adjacent side of each pipe was tapered by 30° to create a V-groove of approximately 60° in accordance with ASME B31 when two pipes are clamped together via a butt-joint configuration. The filler metal employed was a 2.4-m diameter ER308Si (AWS: A5.9) wire with a high content of molybdenum and silicon. The inclusion of nickel and copper in silicon-rich materials with high molybdenum contents considerably increases the corrosion resistance. Table 1 shows the chemical composition of the samples determined via spectrometer analysis (Oxford Foundry Master Pro). The mechanical properties of both materials are presented in Table 2. The weld joint was fabricated using the gas tungsten arc welding process (GTAW) via butt joining. The quality of the weld produced was checked using a liquid dye penetrant and radiographic x-ray tests. The weld joint was subsequently sliced into several small weldments for post weld heat treatment. The welding parameters are detailed in Table 3. The design of the welding joint is shown in Fig. 1. Various PWHT cycles were carried out on four weldments, which were initially heated in an electric furnace to well-defined temperatures of 650, 850, and 1050 °C. These temperatures were

Table 1 Chemical composition of the base metal and filler wire

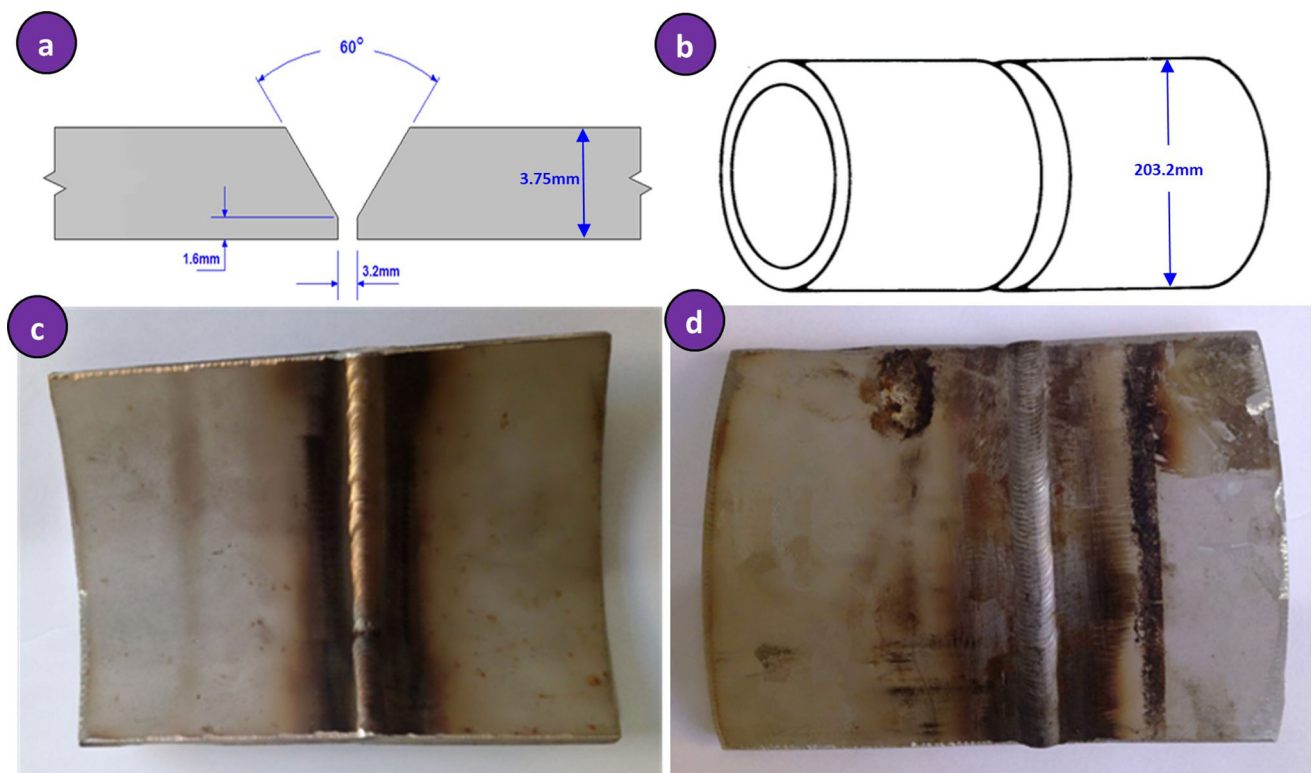
Chemical composition, wt.%												
Material	C	Mn	Si	S	P	Cr	Ni	Mo	Co	Al	Cu	Fe
Base metal AISI 304	0.05	2.03	0.68	...	0.04	18.09	8.15	...	0.21	0.30	0.11	Bal.
Filler wire ER308Si	0.02	1.78	1.07	0.04	0.04	19.38	9.33	0.10	0.18	0.73	0.22	Bal.

Table 2 Mechanical properties of the base metal and filler wire

Material	Ultimate tensile strength UTS, MPa	Yield strength (0.2%) Re _{0.2} , MPa	Elongation E, %	Microhardness, HV
Base Metal AISI 304	645	240	35	160
Filler Wire ER308Si	620	370	36	140

Table 3 GTAW welding parameters

Wire diameter Φ, mm	Welding current I, A	Welding voltage U, V	Welding speed S, mm/min	Heat input H, kJ/mm	Interpass Temperature, T _i °C	Shielding gas, %	Gas flow rate GFR, L/min
2.4	75-85	10-12	70-100	0.61-0.64	150	Ar99.999	12

**Fig. 1** Welding process: (a) schematic of the weld joint, (b) schematic of butt-welded pipes, (c) image of the root-side weld joint, (d) image of the capping-side weld joint

maintained for one hour. Finally, the weldments were quenched in water. The furnace used was a Nabertherm MORE THAN HEAT –30-3000 °C (Germany).

Samples intended for metallographic evaluation were cut across the cross section of the as-welded and post weld-heat-treated weldments. The samples were prepared via standard

procedures consisting of mechanical polishing, followed by polishing with 0.5- μm alumina powder and water to achieve a mirror-like state. The samples were then electrolytically etched in a sulfuric acid solution (H_2SO_4 (5%)) at 4 V for 50 s. The microstructural characteristics of the samples were examined via a light microscope (Nikon Eclipse LV100ND) and a scanning electron microscope (Zeiss. EVO-MA 25) equipped with a microanalysis system (EDS) before and after PWHT. The grain size and ferrite content of the samples were assessed via ImageJ software. The phases in both the BM and WZ of the various welds were qualitatively identified via x-ray diffraction (XRD) with a Cu K α source (using a wavelength of 1.5406 nm, an acquisition step of 0.02 $^\circ$, a voltage V = 30 kV and an intensity I = 10 mA.). The diffractometer utilized was a BRUKER D2 PHASER 2G.

The mechanical properties of the welded joints before and after post weld heat treatment were determined via microhardness and tensile tests. The microhardness tests were carried out via a Wilson VH3300 automatic hardness testing system with a 200-g loading force for a holding time of 15 s. The tensile tests were carried out on a MTS Criterion Model 45 hydraulic test machine. The tensile tests were conducted on subsize samples machined in accordance with the ASTM E8-04 standard (Ref 27).

Electrochemical corrosion tests were performed on both the base metal and weld zone of all the welded joints using the potentiodynamic method with VoltaLab equipment (PGP 201) according to ASTM Standard G61-86 (Ref 28). The test electrolyte was a 3.5 wt.% NaCl solution at room temperature. A conventional three-electrode cell setup was used, with Ag/AgCl as the reference electrode, platinum foil as the auxiliary electrode, and the test samples as the working electrode. During electrochemical testing, thermodynamic equilibrium was achieved at a scan rate of 1 mV/s for 1/2 hour of exposure to generate polarization curves. The sample preparation for the experimental procedure is illustrated in Fig. 2.

4. Results and Discussion

4.1 Weld Microstructure

Figure 3 shows optical micrographs of the BM for all the samples, that is, both the as-welded samples and the samples heat-treated at 650, 850, and 1050 $^\circ\text{C}$. The microstructure of the as-received metal consisted of coarse equiaxed austenite grains (Fig. 3a) with an approximate size of 81.92 μm . Twins were also found in the austenitic matrix (γ). Segregation during solidification causes delta ferrite (δ) to tend to form along austenite grain boundaries (Ref 22, 29-32). During PWHT at 650 $^\circ\text{C}$, the microstructure was partially recrystallized (Fig. 3b), with a γ -grain size of approximately 83.94 μm and a decrease in the twinning rate (Ref 26, 32). Heat treatment at 850 $^\circ\text{C}$ produced a microstructure consisting of equiaxed γ -grains (Fig. 3c) with an average size of 84.29 μm . The appearance of new small γ -grains is attributable to recrystallization. For the sample subjected to PWHT at 1050 $^\circ\text{C}$, the average γ -grain size in the BM increased to 93.30 μm (Fig. 3d), accompanied by a high rate of formation of twins (Ref 26, 33). The reduced grain size can be attributed to fast cooling during water quenching (Ref 26). In conclusion, considerable grain growth did not occur in the 304 BM between 650 and 850 $^\circ\text{C}$.

Slower grain growth was observed at 1050 $^\circ\text{C}$. The quantity of carbon and molybdenum in the base metal has been found to affect grain growth (Ref 32). Figure 4 shows a typical estimate of the γ -grain size in the BM for various samples. The different values are summarized in Table 4.

Figure 5 shows micrographs of the weld zones of the various samples and different post weld heat treatments. These micrographs show a dendritic solidification pattern, where the γ -matrix contains δ dendrites characterized by a skeletal morphology attributed to moderate cooling rates. The majority of δ -ferrite dendrites have widths below 4 μm (Ref 11, 29, 33-37). During the solidification process, the primary δ phase forms from the melt. Then, the γ phase is formed through a peritectic transformation in the three-phase region. The transformation from delta ferrite to austenite is diffusion-controlled. Increasing the cooling rate results in an incomplete transformation, increasing the quantity of the δ phase that is retained in the weld zone (Ref 7, 29, 33). Heat treatment of stainless steel welds causes intricate microstructural changes. Typically, subjecting a material to high temperatures causes the metastable δ -ferrite to dissolve. It has been shown that the dendritic network of ferrite disintegrates and tends to form spherical shapes. The dissolution process is driven by the disparity in the free energy levels of the metastable ferrite and stable transition products (Ref 11, 26, 33). The δ -phase distribution tends to become increasingly uniform as the temperature of heat treatment increases because of the increase in the cooling rate. For the as-welded samples, the initially thin delta ferrite dendrites thicken with heat treatment, especially at 650 $^\circ\text{C}$ (Ref 11, 22). Figure 6 shows a typical estimate of the width of δ -ferrite dendrites in the WZ for all the samples, as listed in Table 5. The δ -ferrite content of all the samples increased during heat treatment. Figure 7 presents a typical estimate of the average rate of formation of δ -ferrite, where the rates for the different samples are shown in Table 6. The increase in the δ -ferrite content results from variations in the thermal cycling and cooling rates (Ref 6, 30, 38).

4.2 XRD and EDS Analysis

Figure 8 shows the XRD patterns for both the base metal and weld zone for all the samples. The diffraction patterns contain peaks corresponding to the austenite γ and delta ferrite δ phases. However, peaks corresponding to chromium carbide or σ phases do not appear in these patterns. An important limitation of the XRD technique is the inability to detect σ or chromium carbide phases at contents below 5% (Ref 22, 31, 39). For this reason, EDS analyses were performed to identify the different phases formed. It is well known that iron, nickel, chromium, nitrogen, carbon and manganese elements have a strong metallurgical influence on phase transformation and carbide or nitride precipitation in stainless steels (Ref 40-42). Chromium carbide precipitates at the grain boundaries in austenitic stainless steel maintained at temperatures between 500 and 900 $^\circ\text{C}$. Therefore, time is an important parameter for the precipitation of chromium carbide. A high cooling rate is essential for preventing the formation of chromium carbide in this critical temperature range, which is commonly observed in GTAW welding (Ref 31, 34, 43-45). Heat treatment between 1040 and 1150 $^\circ\text{C}$ facilitates the dissolution of chromium carbide into the solid solution (Ref 26, 46). Figure 9 and 10 show the results related to the EDS line in the BM and WZ of all the weldments. An analysis of the chemical composition of

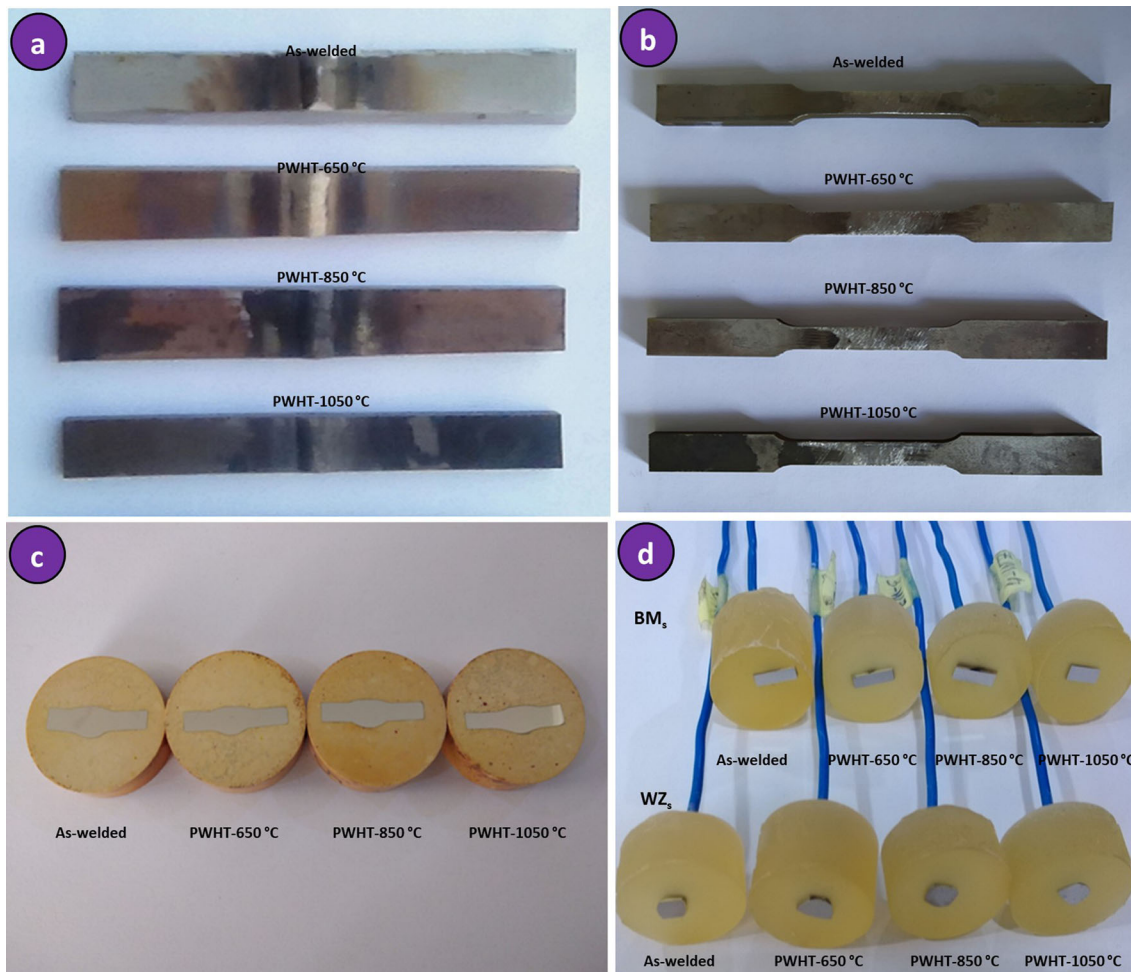


Fig. 2 Preparation of test samples: (a) samples cut for various heat treatments, (b) subsize samples for tensile tests, (c) samples for optical and microhardness tests, (d) samples for electrochemical tests

the base metal 304 and filler metal ER308Si showed no difference in the quantity of Fe. All the EDS spots characterizing the various samples (for both the BM and WZ) showed no increase in the Cr, Ni and Mn contents. This observation suggests the absence of intermetallic precipitates, particularly chromium carbides and the presence of traces of manganese oxide in the base metal for the sample subjected to PWHT at 650 °C.

4.3 Microhardness Testing

The microstructure of materials is a determining factor of their mechanical properties. Figure 11 presents the microhardness profiles of the various samples. The Vickers microhardness was determined to be 170 ± 10 HV for the base metal samples, with the exception of the sample subjected to PWHT at 650 °C, which had the highest base metal microhardness (approximately 190 HV) because of partial recrystallization of the microstructure and a high content of twins (Ref 47, 48). The microhardness of the HAZs of various samples were similar and slightly greater than that of the base metal, except for the sample subjected to PWHT at 850 °C, which had a high microhardness (approximately 210 HV) because of grain refinement and the possible formation of chromium carbides. All the weld zones (WZs) had lower microhardness values

(approximately 150 ± 10 HV) than the heat-affected zone (HAZ) and base metal (BM). This result was obtained because of the high δ -ferrite content of the weld zone (Ref 22, 39, 49). Unlike the microhardness of the as-welded samples, the microhardness of the weld metal decreases at a heat treatment temperature of 650 °C and increases above 850 °C (Ref 22). This variation in the microhardness results from the content and distribution of delta ferrite, the segregation of alloying elements (such as Cr and Ni), and the change in the dislocation rate caused by different cooling rates during post weld heat treatment (Ref 1, 22, 32, 50-52). Finally, the optimal and most stable microhardness profile was measured for the sample subjected to PWHT at 1050 °C.

4.4 Tensile Testing

The ultimate tensile strength (UTS) and elongation (E) values of the samples are shown as bar graphs in Fig. 12a. The yield strength and ultimate tensile strength are presented in Table 7. These results show that the maximum UTS of 670.20 MPa was measured for the as-welded joint. The PWHT treatment resulted in a remarkable reduction in the UTS, which was measured as 614.70 and 559.70 MPa for the samples subjected to PWHT at 650 and 850 °C, respectively. This decrease in strength is attributed to the decrease in the overall

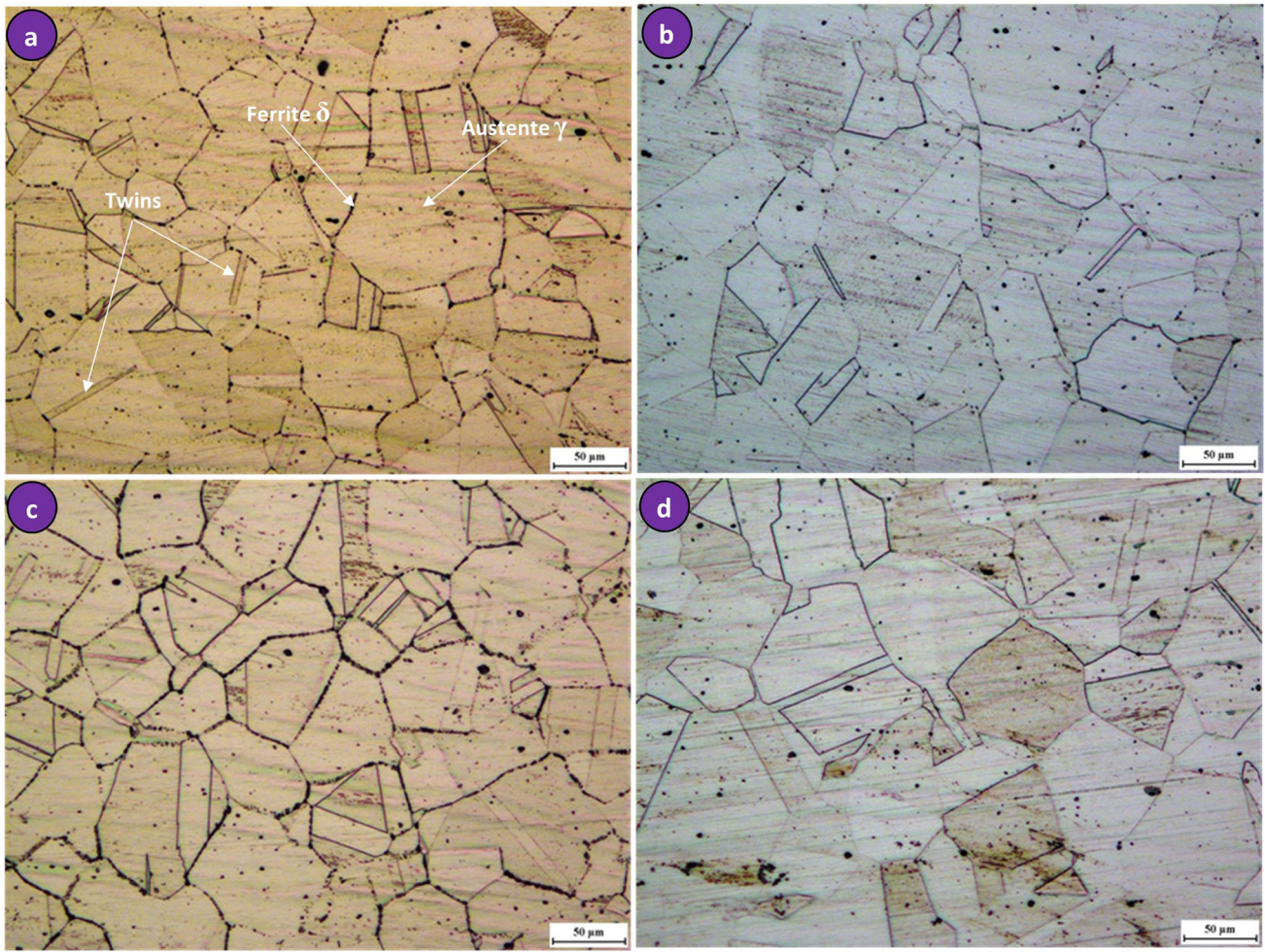


Fig. 3 Optical micrographs of 304 austenitic stainless steel base metals: (a) as-received and subjected to PWHT at (b) 650 °C, (c) 850 °C, and (d) 1050 °C

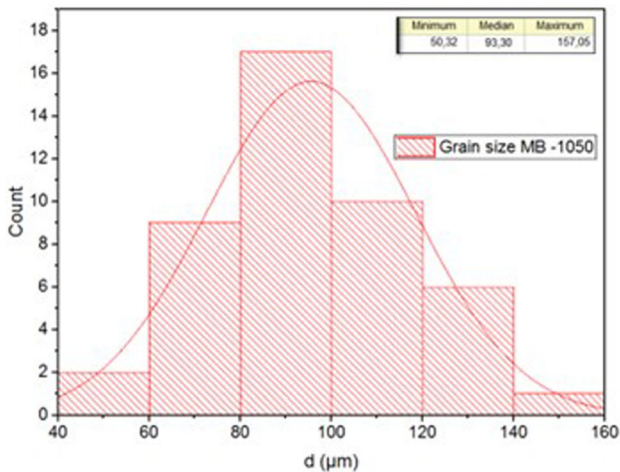


Fig. 4 Typical estimate of the grain size of the base metal for all weldments

microhardness across the weld and the evolution of the precipitates. The UTS of the sample subjected to PWHT at 1050 °C was lower than that of the as-welded sample but greater than that of the sample subjected to PWHT at 850 °C

(Ref 22, 47, 52). The sample subjected to PWHT at 650 °C had a greater measured ductility (20.87%) than the other samples. These results are attributed to partial recrystallization of the microstructure, a high formation rate of twins and variation in the hardness along the welded joint (Ref 46, 52, 53). Figure 12b shows the fractured as-welded and PWHT samples. All the samples fractured at the center of the weld zone. This result determined by analyzing the fracture morphology of the base metal (Fig. 13), which was completely different from that of the WZ. Figure 13 shows ductile dimples, shear fractures, many microvoids and small cleavage facets in the WZ.

The efficiency of the welded joint was calculated using the following equation (Ref 52):

$$\text{Weld efficiency} = \frac{\text{Ultimate tensile strength of welded joint}}{\text{Ultimate tensile strength of as-received base metal}}$$

Table 2 shows that the UTS of the base metal was approximately 645 MPa. The maximum joint efficiency was determined to be approximately 104% for the joint in the as-welded state. Similarly, the joint subjected to PWHT at 650 °C exhibited an acceptable efficiency of approximately 95%. However, the samples subjected to heat treatment at higher

Table 4 Average grain size of the BM for all samples

Sample	As-welded	PWHT-650 °C	PWHT-850 °C	PWHT-1050 °C
Grains size (μm)	81.92	83.94	84.29	93.30

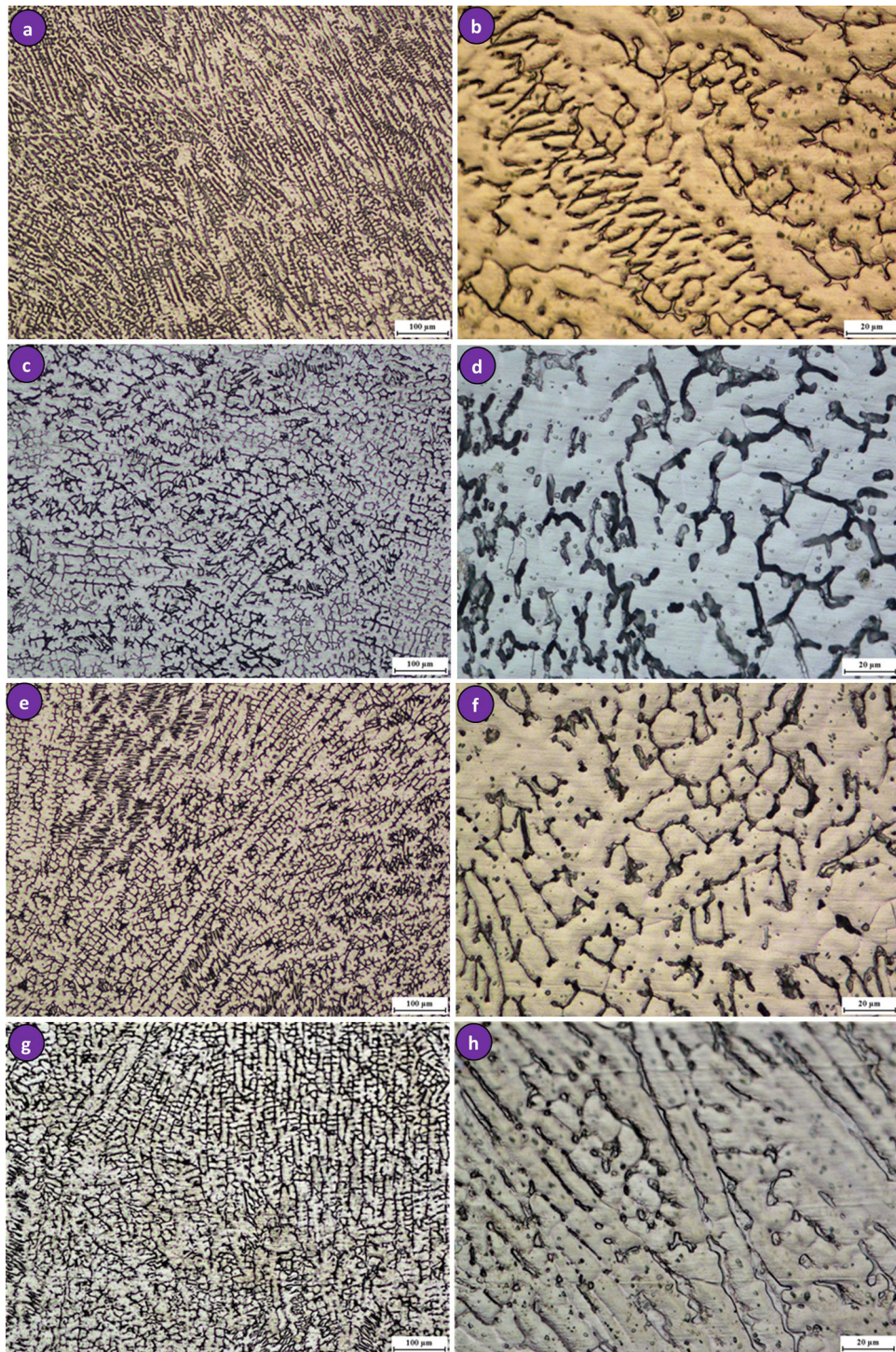


Fig. 5 Optical micrographs of the weld zone for all weldments: (a, b) as-welded and subjected to PWHT at (c, d) 650 °C, (e, f) 850 °C, and (g, h) 1050 °C

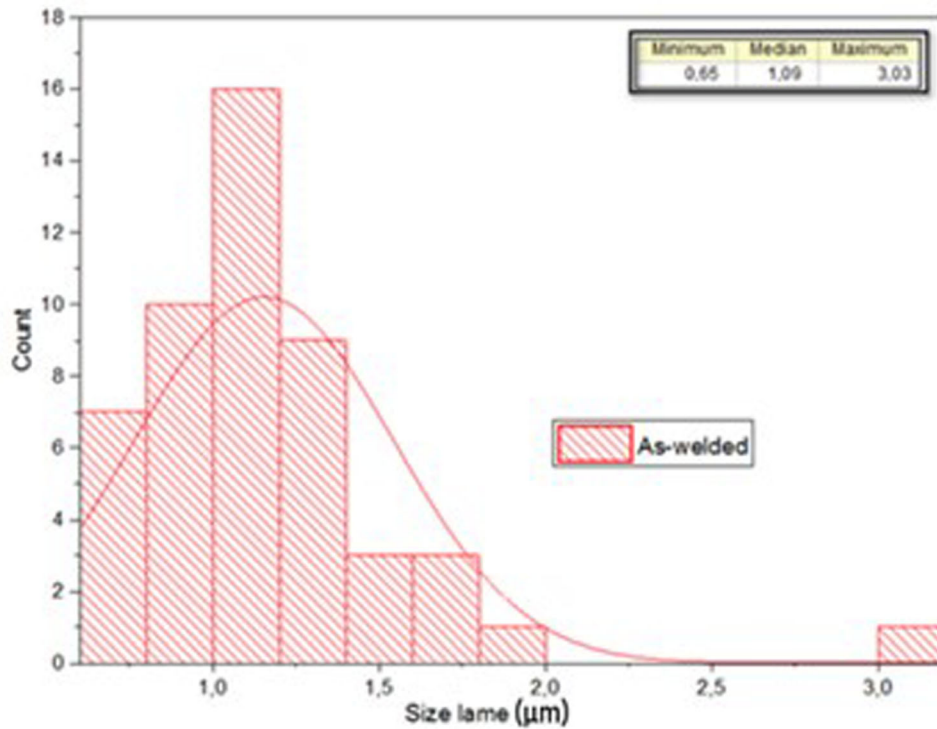


Fig. 6 Typical estimate of average width of delta ferrite dendrites δ in the WZ for all weld samples

Table 5 Width of δ -ferrite dendrites in the WZ for all samples

Sample	As-welded	PWHT-650 °C	PWHT-850 °C	PWHT-1050 °C
Width (μm)	1.09	3.02	1.53	2.12

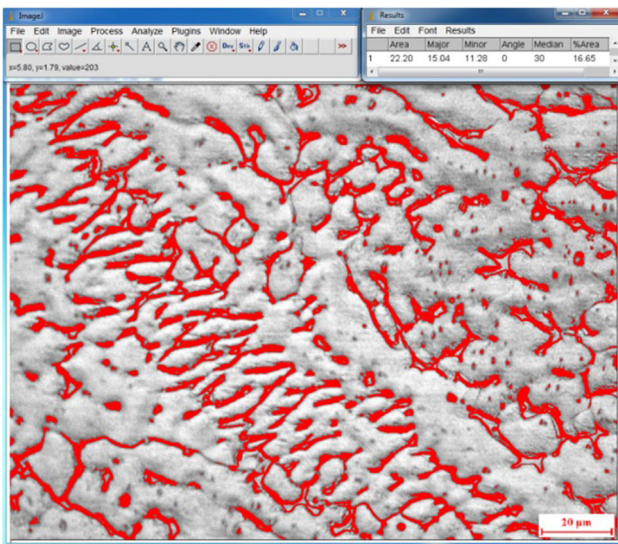


Fig. 7 Typical estimate of the average rate of formation of delta ferrite (δ) in the WZ for all weld samples

temperatures, specifically at 850 and 1050 °C, had lower efficiencies of approximately 87% and 90%, respectively.

Figure 14 shows SEM fractographs of all the samples after the tensile tests. The top views shown in Fig. 14(a), (c), (e), and

(g) shows the coexistence of both cleavage and ductile regions. The fracture surface is distinguished primarily by the presence of ductile dimples, tear ridges, shear failure, and cleavage facets. The fracture morphology of the sample after the tensile test sample (shown in Fig. 14b, d, f, and h) reveals the presence of dimples that are not fully equiaxed and appear slightly elongated. The fractography of the as-welded joint (Fig. 14b) contains both cleavage facets and small to medium-sized ductile dimples. However, the dimples are the dominant characteristics of the fracture surfaces (Ref 1, 29, 46, 52, 54-57). By contrast, for the sample subjected to PWHT at 650 °C (Fig. 14d), there was an increase in the number of transgranular cleavage facets and the size of the dimples detected on the fracture surface. This result suggests a higher level of flexibility and elongation for this sample compared to the other samples (Ref 47, 57-59). For the sample subjected to PWHT at 850 °C (as shown in Fig. 14f), the fracture exhibited ductility, as characterized by the presence of small dimples that were produced during grain refinement. The fracture surface exhibited cleavage facets and tear ridges, indicating low flexibility of the sample (Ref 15, 52, 57-61). The final fracture zone, as observed in the sample subjected to PWHT at 1050 °C (Fig. 14h), exhibited the distinct features of ductile fracture. This fracture contained medium-sized dimples that were somewhat shallow compared with the fracture of the as-welded sample (Ref 55, 62).

Table 6 Rate of formation of δ -ferrite in the WZ for all samples

Sample	As-welded	PWHT-650 °C	PWHT-850 °C	PWHT-1050 °C
δ (%)	16.65	24.88	17.25	18.02

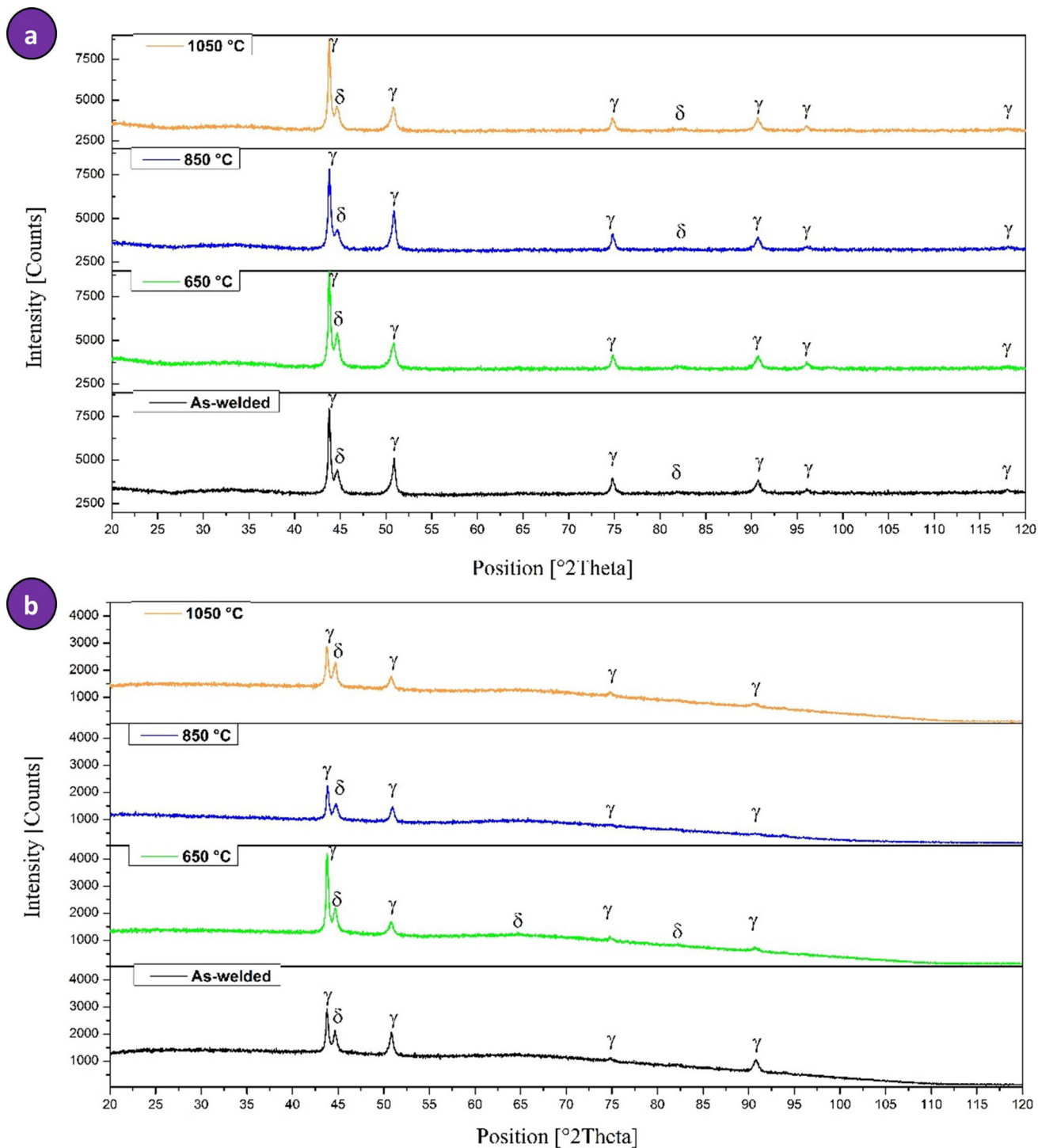


Fig. 8 XRD patterns of all the weldments in the (a) base metal (BM) and (b) weld zone (WZ)

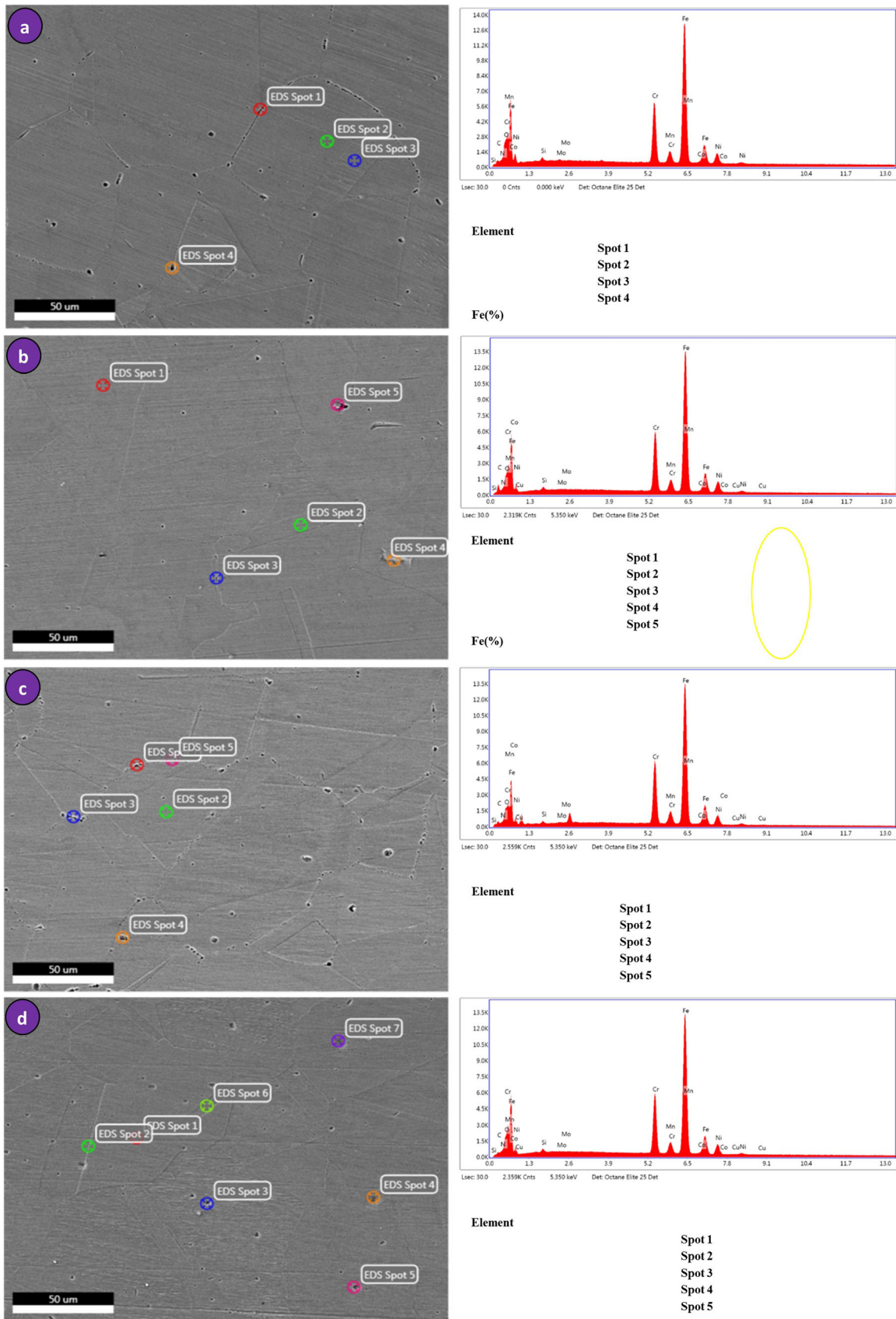


Fig. 9 SEM/EDS images of the BMs of all the samples: (a) as-welded and subjected to PWHT at (b) 650 °C, (c) 850 °C, and (d) 1050 °C

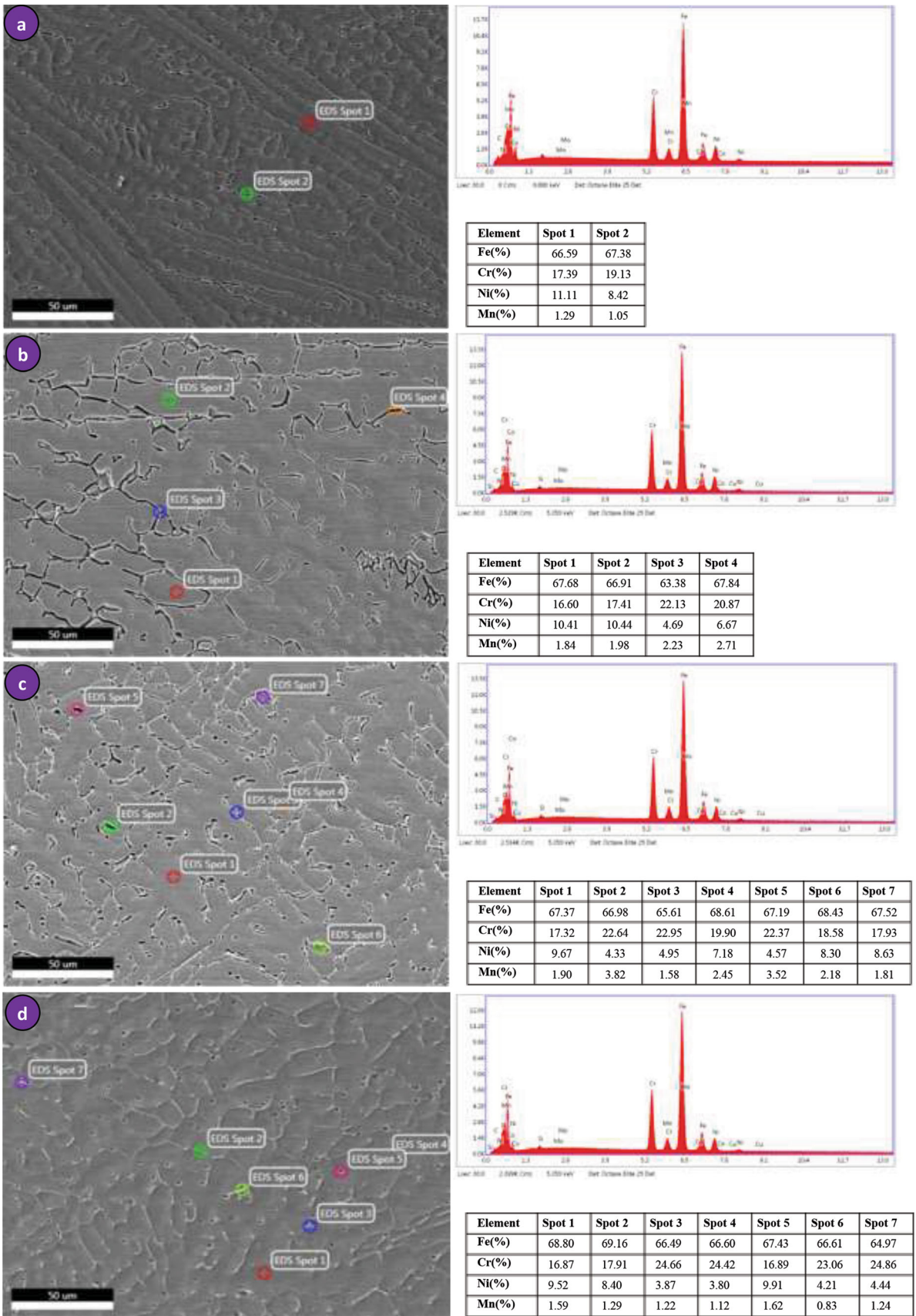


Fig. 10 SEM/EDS images showing the WZ of all the samples: (a) as-welded and subjected to PWHT at (b) 650 °C, (c) 850 °C, and (d) 1050 °C

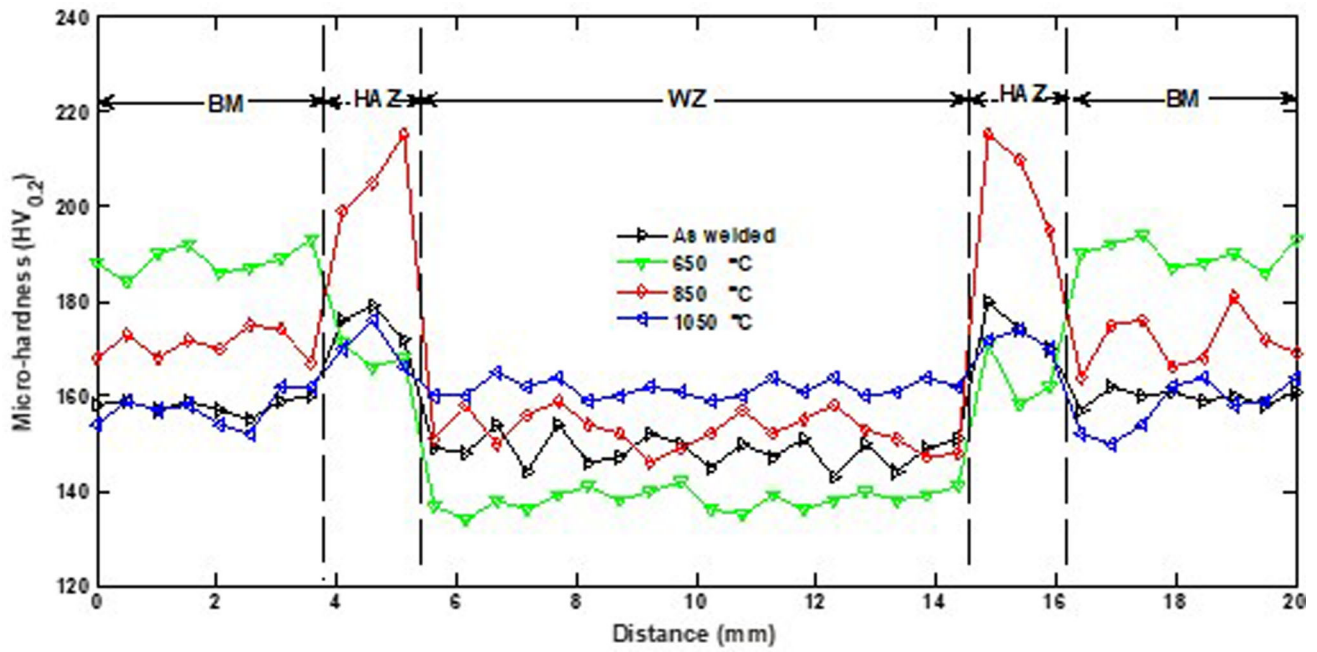


Fig. 11 Microhardness profiles of as-welded and heat-treated samples

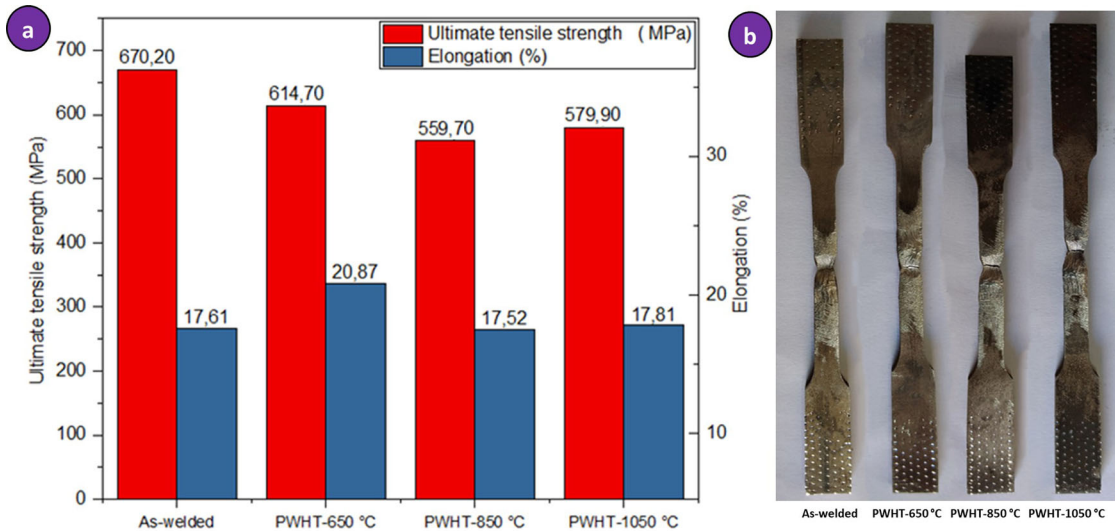


Fig. 12 Results of tensile tests on welded joints subjected to different PWHT treatments: (a) bar graphs of the ultimate tensile strength and elongation and (b) fracture zones of subsized samples after tensile testing

Table 7 Tensile properties of the welded and heat-treated samples

Specimen	Ultimate tensile strength, MPa	Yield strength 0.2%, MPa	Elongation, %	Joint efficiency, %
As-welded	670.20	290	17.61	104
650°C	614.70	250	20.87	95
850°C	559.70	225	17.52	87
1050°C	579.90	260	17.81	90

4.5 Corrosion Behavior

The corrosion susceptibility of the base metal and weld zone of all the samples (with and without PWHT in a 3.5% NaCl

solution at room temperature) was reflected in the potentiodynamic polarization curves (Fig. 15). Polarization curves offer insights into how the microstructure of any zone in the weld joint influences corrosion resistance. The cathodic parts of all

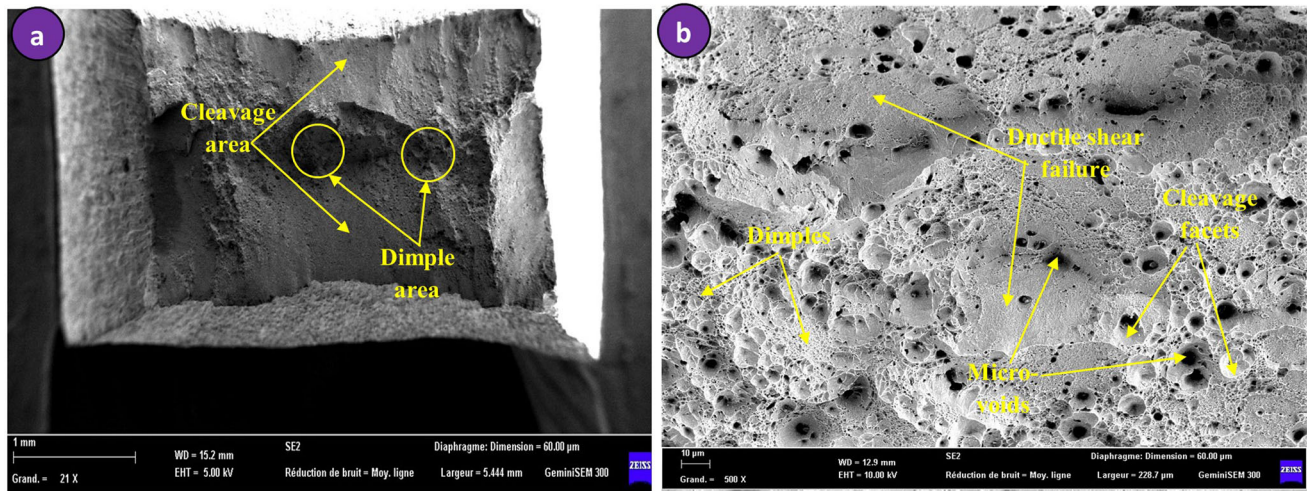


Fig. 13 SEM fractographs of the 304 base metal after tensile testing: (a) top view and (b) fracture morphology

the curves tended to shift toward the negative potential domain. This result was obtained because of the rapid dissolution occurring on the metallic surface (Ref 7, 26). Table 8 shows the values of various electrochemical parameters, such as the corrosion current density (i_{corr}), corrosion potential (E_{corr}), and corrosion rate (V_{corr}), that were determined from these curves.

Comparing the aforementioned values against the corresponding values of these parameters for the base metal revealed that the as-welded sample exhibited greater corrosion resistance with a lower corrosion current density, higher corrosion potential and wider passive region than the heat-treated samples. With the exception of the sample subjected to PWHT at 1050 °C, the heat-treated samples also exhibited acceptable corrosion resistance. This result can be explained in terms of the microstructure, morphology and coarser austenite grain size of the heat-treated samples. For the sample subjected to PWHT at 650 °C, the microstructure partially recrystallized, whereas new small grains appeared in the sample subjected to PWHT at 850 °C, which is attributed to recrystallization (Ref 26, 38). However, PWHT up to 850 °C, especially PWHT at 650 °C, reduced the corrosion current density and increased the corrosion potential, increasing the corrosion resistance of the weld zone. Rapid cooling and the resulting high dislocation density (Ref 63, 64) induced the dissolution of the precipitates, which decreased the impact of galvanic corrosion between the precipitates and the matrix. Consequently, more paths were available for chromium migration to the surface, where corrosion products of Fe_2O_3 and Cr_2O_3 formed. The resulting fine-grained microstructures made the developed surface oxides compact, impermeable, and uniform. This behavior explains the strong electrochemical stability that has been reported for heat-treated samples (Ref 1, 26, 32, 50, 51, 65, 66). The EDS studies clearly revealed that the chromium content was reduced by PWHT at 650 °C. This result may confirm the mechanism described above, which results in a reduction in the concentration of chromium in δ -ferrite. Finally, when comparing the base metal and the weld zone for the as-welded sample, the base metal shows better corrosion resistance properties.

5. Conclusion

The following conclusions were drawn from the experimental results:

- (1) For the as-welded sample, the BM had a microstructure with equiaxed austenite grains of varying sizes, limited by grain boundaries with a size of approximately 81.92 μm . The grain boundaries had a minor content of δ -ferrite, with twin crystals distributed in the γ -matrix. The WZ exhibited dendritic solidification, where the δ -ferrite phase had a skeletal morphology that was immersed in the γ -matrix.
- (2) PWHT induced changes in the BM microstructure, such as coarsening of the γ -grains and changes in the rate of formation of twin crystals. PWHT treatment at 650 °C caused partial recrystallization with a decrease in rate of formation of twin crystals. Further heat treatment at 850 °C caused recrystallization with the appearance of new small γ -grains. The average γ -grain size of the BM was 93.30 μm , a notable increase over that of the as-welded sample, and was accompanied by a high rate of formation of twins.
- (3) Measurements of the ferrite content of the WZ revealed an increase in the δ fraction after PWHT, especially at 650 °C. The δ -phase distribution tended to become increasingly uniform as the temperature of heat treatment increased because of the increase in the cooling rate.
- (4) The microhardness profiles revealed that PWHT decreased the hardness of the WZ for all the samples (to approximately 150 ± 10 HV). An increase in the hardness of the BM was observed for the sample subjected to PWHT at 650 °C because of partial recrystallization of the microstructure and a high rate of formation of twins. For the sample subjected to PWHT at 1050 °C, the hardness changed monotonically across the weld.
- (5) Tensile tests revealed that the failure of all the samples occurred in the WZ by a mixed-mode failure mecha-

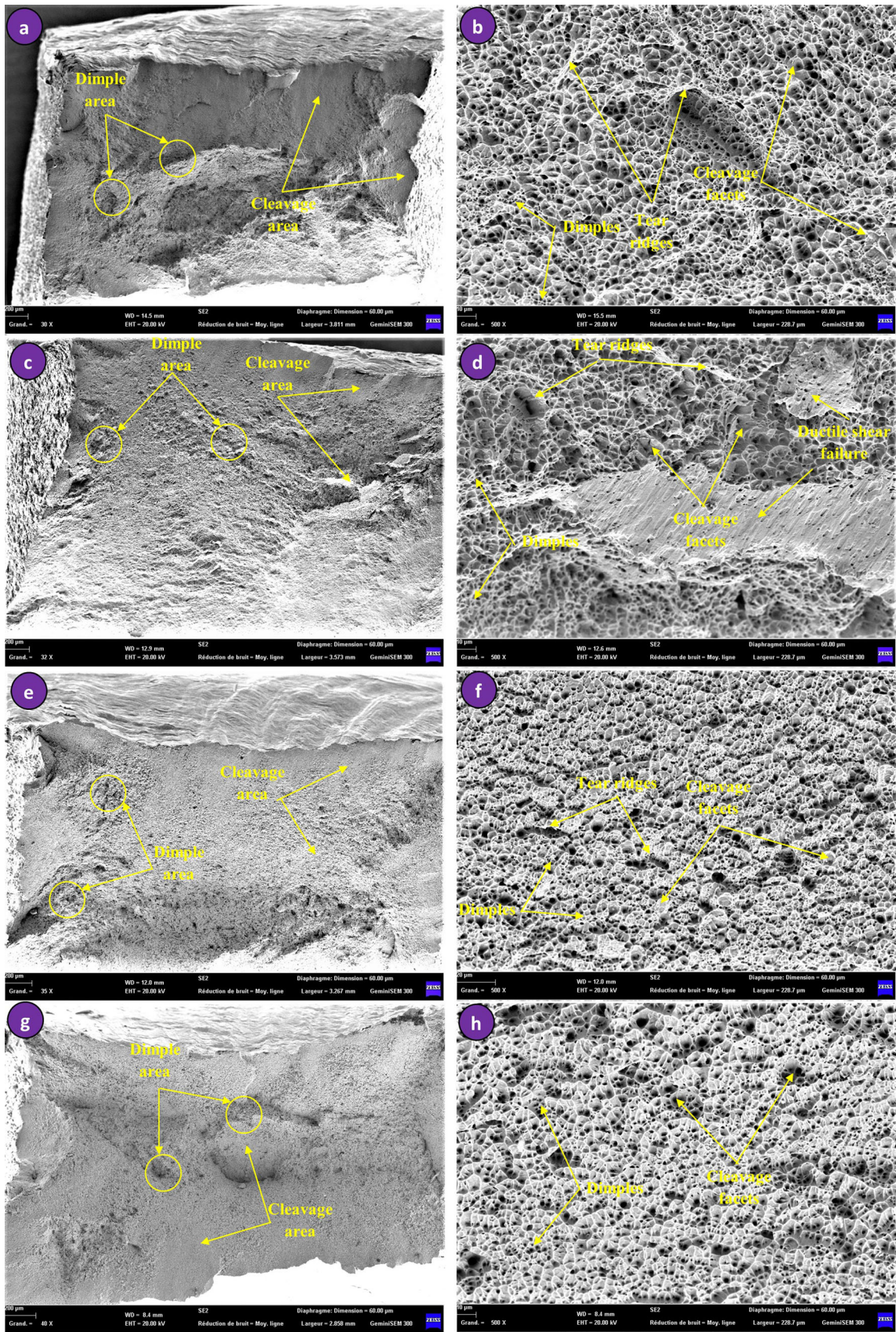


Fig. 14 SEM fractographs of samples subjected to tensile tests: (a, b) as-welded and subjected to PWHT at (c, d) 650 °C, (e, f) 850 °C, and (g, h) 1050 °C

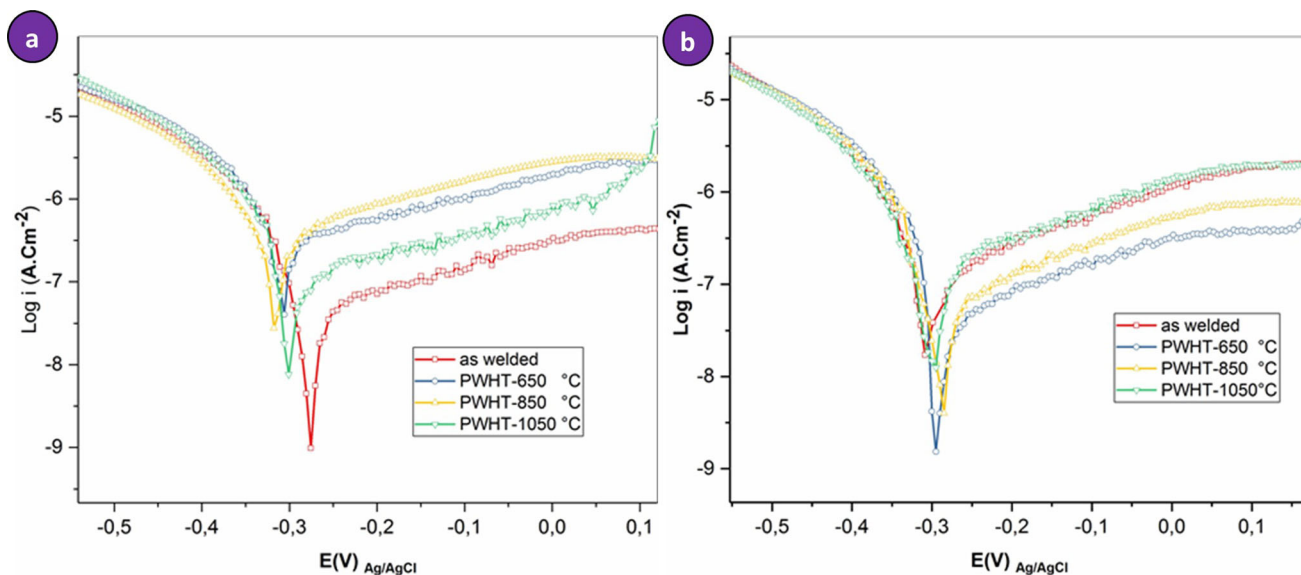


Fig. 15 Potentiodynamic polarization curves for all weldments obtained in a 3.5% NaCl solution at room temperature: (a) base metal and (b) weld zone

Table 8 Electrochemical corrosion parameters determined from potentiodynamic polarization curves of various samples obtained in a 3.5% NaCl solution at room temperature

Area	Sample	i_{corr} $\mu\text{A}/\text{cm}^2$	E_{corr} mV	V_{corr} $\mu\text{m}/\text{y}$
BM	As-welded	0.05	-277.36	0,62
	PWHT-650 °C	0.51	-304.72	5,98
	PWHT-850 °C	1.01	-315.81	11,72
	PWHT-1050 °C	0.20	-301.65	2,27
WZ	As-welded	0,61	-308.31	2,96
	PWHT-650 °C	0.05	-295.14	0,62
	PWHT-850 °C	0,10	-282.77	1,16
	PWHT-1050 °C	0,23	-281.96	2,71

nism. The highest UTS of 670.2 MPa was measured for the as-welded joint, but the highest elongation (20.87%) was measured for the sample subjected to PWHT at 650 °C.

- (6) An electrochemical analysis showed that the corrosion potential of the BM was greater for the as-welded sample (-277.36 mV) than the heat-treated samples (-304.72, -315.81 and -301.65 mV). These findings indicate that the corrosion resistance of the as-welded BM had superior corrosion resistance to the heat-treated BMs. PWHT up to 850 °C, especially at 650 °C, increased the corrosion resistance of the weld zone because of a reduction in galvanic corrosion between δ -ferrite and the γ -matrix resulting from the depletion of Cr in δ -ferrite and Cr migration toward the surface.

Acknowledgments

The authors wish to express their sincere appreciations to the Research Center in Industrial Technologies (CRTI).

Authors Contribution

All authors contributed to the research, writing, and reviewing of the paper.

Conflict of interests

The authors declare no competing interests.

Ethics approval

Not applicable.

Consent to participate

Not applicable.

Consent to publish

The authors give all the rights to publish the material presented in this work.

References

- H.S. Surkar, A. Kumar, S. Sirohi, S.M. Pandey, A. Świerczyńska, D. Fydrych and C. Pandey, A Dissimilar Welded Joint of Grade 92 Steel and AISI 304L Steel Obtained Using IN82 Buttering and IN617 Filler: Relationship of Microstructure and Mechanical Properties, *Arch. Civ. Mech. Eng.*, 2024, **24**(2), p 109.
- G. Dak, K. Guguloth, R.S. Vidyarthi, D. Fydrych and C. Pandey, Creep Rupture Study of Dissimilar Welded Joints of P92 and 304L Steels, *Weld. Int.*, 2024 <https://doi.org/10.1007/s40194-024-01757-x>
- J.R. Davis, *Corrosion of Weldments Corrosion of Austenitic Stainless Steel Weldments*, ASM International, USA, 2006, p 43–66
- S. Kumar, A.S. Shahi, V. Sharma and D. Malhotra, Effect of welding Heat Input and Post-Weld Thermal Aging on the Sensitization and Pitting Corrosion Behavior of AISI 304L Stainless Steel Butt Welds, *J. Mater. Eng. Perform.*, 2021, **30**, p 1619–1640.
- F.J. dos Santos, G.B. Dutra and T.V. da Cunha, Microstructural and Mechanical Evaluation of a Dissimilar Joining Between SAE 1020 and AISI 304 Steel Obtained via Ultra-High-Frequency-Pulsed GTAW, *J. Braz. Soc. Mech. Sci. & Eng.*, 2019, **41**, p 1–10.

6. G.R. Mirshekari, E. Tavakoli, M. Atapour and B. Sadeghian, Microstructure and Corrosion Behavior of Multipass Gas Tungsten Arc Welded 304L Stainless Steel, *Mater. Des.*, 2014, **55**, p 905–911.
7. A. Sriba and J.B. Vogt, Galvanic Coupling Effect on Pitting Corrosion of 316L Austenitic Stainless Steel Welded Joints, *Met. Mater. Int.*, 2021, **27**, p 5258–5267.
8. M. Kumar, A. Sharma, A.S. Shahi, A Sensitization Studies on the Metallurgical and Corrosion Behavior of AISI 304 SS Welds, in *Advances in Manufacturing Processes: Select Proceedings of ICEMMM*, (Springer, 2018), pp. 257–265
9. F. Liu, Y.H. Hwang and S.W. Nam, The Effect of Post Weld Heat Treatment on the Creep-Fatigue Behavior of Gas Tungsten Arc Welded 308L Stainless Steel, *Mater. Sci. Eng. A*, 2006, **427**, p 35–41.
10. W. Tian, N. Du, S. Li, S. Chen and Q. Wu, Metastable Pitting Corrosion of 304 Stainless Steel in 3.5% NaCl Solution, *Corros. Sci.*, 2014, **85**, p 372–379.
11. J. Yan, M. Gao and X. Zeng, Study on Microstructure and Mechanical Properties of 304 Stainless Steel Joints by TIG, Laser and Laser-TIG Hybrid Welding, *Opt. Lasers Eng.*, 2010, **48**, p 512–517.
12. P. De Tiedra, Ó. Martín and M. López, Combined Effect of Resistance Spot Welding and Post-Welding Sensitization on the Degree of Sensitization of AISI 304 Stainless Steel, *Corros. Sci.*, 2011, **53**, p 2670–2675.
13. A. Kellai, S. Kahla, S. Dehimi, L. Kaba and Z. Boutaghou, Effect of Post Weld Heat Treatment on the Microstructure and Mechanical Properties of a Gas-Tungsten-Arc-Welded 304 Stainless Steel, *Int. J. Adv. Manuf. Technol.*, 2022, **121**, p 8171–8186.
14. M. Dadfar, M.H. Fathi, F. Karimzadeh, M.R. Dadfar and A. Saatchi, Effect of TIG Welding on Corrosion Behavior of 316L Stainless Steel, *Mater. Lett.*, 2007, **61**, p 2343–2346.
15. J. Xin, C. Fang, Y. Song, J. Wei, S. Xu and J. Wu, Effect of Post Weld Heat Treatment on the Microstructure and Mechanical Properties of ITER-Grade 316LN Austenitic Stainless Steel Weldments, *Cryogenics*, 2017, **83**, p 1–7.
16. A. Adesanmi, I.M.B. Omiogbemi, N.S. Gukop, A.K. Gummedi, S.M. Negash, I.M. Dagwa, Microstructural and Corrosion Characteristics of a Heat Treatable Stainless-Steel Weldments, in *IOP Conference Series: Materials Science and Engineering*, vol. 1185, (IOP Publishing, 2021), p. 012030
17. U.K. Mudali, R.K. Dayal, J.B. Gnanamoorthy and P. Rodriguez, Influence of Thermal Aging on the Intergranular Corrosion Resistance of Types 304LN and 316LN Stainless Steels, *Metall. Mater. Trans. A*, 1996, **27**, p 2881–2887.
18. M. Vach, T. Kuniková, M. Dománková, P. Ševc, L. Caplovic, P. Gogola and J. Janovec, Evolution of Secondary Phases in Austenitic Stainless Steels During Longterm Exposures at 600, 650 and 800°C, *Mater. Charact.*, 2008, **59**, p 1792–1798.
19. S. Kumar and A.S. Shahi, Effect of Heat Input on the Microstructure and Mechanical Properties of Gas Tungsten Arc Welded AISI 304 Stainless Steel Joints, *Mater. Des.*, 2011, **3**, p 3617–3623.
20. Z. Zhang, H. Jing, L. Xu, Y. Han, L. Zhao and X. Lv, Effect of post-Weld Heat Treatment on Microstructure Evolution and Pitting Corrosion Resistance of Electron Beam-Welded Duplex Stainless Steel, *Corros. Sci.*, 2018, **141**, p 30–45.
21. P. Mayr, C. Schlacher, J.A. Siefert and J.D. Parker, Microstructural Features, Mechanical Properties and High Temperature Failures of Ferritic to Ferritic Dissimilar Welds, *Int. Mater. Rev.*, 2018, **64**, p 1–26.
22. T.H. Nam, E. An, B.J. Kim, S. Shin, W.S. Ko, N. Park, N. Kang and J.B. Jeon, Effect of Post Weld Heat Treatment on the Microstructure and Mechanical Properties of a Submerged-Arc-Welded 304 Stainless Steel, *Metals.*, 2018, **8**, p 13–26.
23. B.M. Sim, T.S. Hong, M.A.Z. Hanim, E.J.N. Tchan and M.K. Talari, The Influence of Post Weld Heat Treatment Precipitation on Duplex Stainless Steels Weld Overlay Towards Pitting Corrosion, *Materials.*, 2019, **12**, p 1–11.
24. D. Malhotra and A.S. Shahi, Metallurgical Behavior and Corrosion Performance of Ti+ Nb Stabilized Austenitic Stainless Steel Welds, *J. Mater. Eng. Perform.*, 2023, **32**(2), p 544–561.
25. M. Kumar, A. Babbar, A. Sharma, A.S. Shahi, Effect of Post Weld Thermal Aging (PWTA) Sensitization on Micro-Hardness and Corrosion Behavior of AISI 304 Weld Joints, in *Journal of Physics: Conference Series*, vol. 1240, (IOP Publishing, 2019), p. 012078
26. T.E. Abioye, I.S. Omotehinse, I.O. Oladele, T.O. Olugbade and T.I. Ogedengbe, Effects of Post-Weld Heat Treatments on the Microstructure, Mechanical and Corrosion Properties of Gas Metal Arc Welded 304 Stainless Steel, *World. J. of Eng.*, 2020, **17**, p 87–96.
27. ASTM E8–04, Standard Test Methods for Tension Testing of Metallic Materials, 2008
28. ASTM standard G61–86, *Standard Test Method for Conducting Cyclic Potentiodynamic Polarization Measurements for Localized Corrosion Susceptibility of Iron-, Nickel-, or Cobalt-Based Alloys*, Annual book of *ATSM Standards*, ASTM International, Philadelphia, 2014
29. P.V.S.S. Sridhar, P. Biswas and P. Mahanta, Effect of Process Parameters on Bead Geometry, Tensile and Microstructural Properties of Double-Sided Butt Submerged Arc Welding of SS 304 Austenitic Stainless Steel, *J. Braz. Soc. Mech. Sci & Eng.*, 2020, **42**, p 1–15.
30. M.A. Ghadam Dezfuli, R. Dehmolaei and S.R. Alavi Zaree, Microstructural Aspects of 304 Stainless Steel Weld Joints with the Simultaneous Application of Electromagnetic Vibration, *Metallogr. Microstruct. Anal.*, 2019, **8**, p 226–232.
31. A. Khodadadi, M. Shamanian and F. Karimzadeh, Microstructure and Mechanical Properties of Dissimilar Friction Stir Spot Welding Between St37 Steel and 304 Stainless Steel, *J. Mater. Eng. Perform.*, 2017, **26**, p 2847–2858.
32. G. Dak and C. Pandey, Experimental Investigation on Microstructure, Mechanical Properties, and Residual Stresses of Dissimilar Welded Joint of Martensitic P92 and AISI 304L Austenitic Stainless Steel, *Int. J. Press. Ves. Pip.*, 2021, **194**, 104536
33. J. Kangazian and M. Shamanian, Multiresponse Optimization of Pulsed-Current Gas Tungsten Arc Welding (PCGTAW) for AISI 304 Stainless Steel to St 52 Steel Dissimilar Welds, *Metallogr. Microstruct. Anal.*, 2016, **5**, p 1–10.
34. S. Bezawada, Mechanical and Microstructural Characteristics of Gas Tungsten Arc Welded Similar and Dissimilar Joints of SS-316L and Hastelloy C276, *Trans. Indian Inst. Met.*, 2021, **74**, p 1623–1637.
35. R. Barbosa Goncalvesa, P.H.D. de Araujoa, F.J.V. Bragab, L.A.H. Terronesc and R.P. da Rocha Paranhos, Effect of Conventional and Alternative Solution and Stabilizing Heat Treatment on the Microstructure of a 347 Stainless Steel Welded Joint, *Weld. Int.*, 2016, **31**, p 196–205.
36. L.G. Galdino, S.F. Rodrigues, C. Aranas, G.S. Reis and V.A. Ferraresi, The Effect of Purge Gas Condition on the Amount of Ferrite in Tubular AISI 304 Stainless Steel During Welding, *J. Braz. Soc. Mech. Sci & Eng.*, 2018, **40**, p 1–15.
37. X. Lin, Q. Peng, Y. Han, E.H. Han and W. Ke, Effect of Thermal Ageing and Dissolved Gas on Corrosion of 308L Stainless Steel Weld Metal in Simulated PWR Primary Water, *J. Mater. Sci. Technol.*, 2022, **96**, p 308–324.
38. S. Sharma, R.V. Taiwade, A. Yadav and H. Vashishtha, Influence of Fillers and Welding Processes on the Microstructural Evolution, Mechanical Properties and Corrosion Behavior Of Dissimilar Hastelloy C-22/AISI 321 Joints, *Mater. Res. Express.*, 2019, **6**, p 1–14.
39. P. Kumar, A.N. Sinha, C.K. Hirwani, M. Murugan, A. Saravanan and A.K. Singh, Effect of Welding Current in TIG Welding 304L Steel on Temperature Distribution, Microstructure and Mechanical Properties, *J. Braz. Soc. Mech. Sci & Eng.*, 2021, **43**, p 1–20.
40. M. Lomozik, Effect of the Welding Thermal Cycles on the Structural Changes in the Heat Affected Zone and on its Properties in Joints Welded in Low-Alloy Steels, *Weld. Int.*, 2000, **14**, p 845–850.
41. A. Kellai, S. Kahla, S. Dehimi, B. Babes, Microstructural and Mechanical Properties of Welding and Thermal Spraying Coatings on Ductile Cast Iron, in *Defect and Diffusion Forum*, vol. 406, (Trans. Tech. Publications Ltd., 2021), pp. 300–311
42. M.F. Benlamouar, M. Hadji, R. Badji, N. Bensaid, T. Saadi, Y.L. dit Laksir and S. Senouci, Optimization of TIG Welding Process Parameters for X70–304L Dissimilar Joint Using Taguchi Method, *Solid State Phenom.*, 2019, **297**, p 51–61.
43. J. Liu, H.P. Duarte and S. Kou, Evidence of Back Diffusion Reducing Cracking During Solidification, *Acta Mater.*, 2017, **122**, p 47–59.
44. C. Wang, Y. Yu, J. Yu, Y. Zhang, Y. Zhao and Q. Yuan, Microstructure Evolution and Corrosion Behavior of Dissimilar 304/430 Stainless Steel Welded Joints, *J. Manuf. Processes.*, 2020, **50**, p 183–191.
45. B. Weiss and R. Stickler, Phase Instabilities During High Temperature Exposure of 316 Austenitic Stainless Steel, *Metall. Mater. Trans.*, 1972, **3**, p 851–866.
46. Y. Aghayar, A. Naghashzadeh and M. Atapour, An Assessment of Microstructure and Mechanical Properties of Inconel 601/ 304 Stainless Steel Dissimilar Weld, *Vacuum*, 2021, **184**, p 1–10.

47. J. Yang, Y. Wang, F. Li, W. Huanga, G. Jing, Z. Wang and X. Zeng, Weldability, Microstructure and Mechanical Properties of Laserwelded Selective Laser Melted 304 Stainless Steel Joints, *J. Mater. Sci. Technol.*, 2019, **35**, p 1817–1824.
48. W. Chuaiphon and L. Srijaroenpramong, Effect of Welding Speed on Microstructures, Mechanical Properties and Corrosion Behaviour of GTA-Welded AISI 201 Stainless Steel Sheets, *J. Mater. Process. Technol.*, 2014, **214**, p 402–408.
49. G.R. Mirshekari, A. Saatchi, A. Kermanpur and S.K. Sadrnezhad, Effect of Post Weld Heat Treatment on Mechanical and Corrosion Behaviors of NiTi and Stainless Steel Laser-Welded Wires, *J. Mater. Eng. Perform.*, 2016, **25**, p 2395–2402.
50. W. Wang, X. Meng, W. Dong, Y. Xie, X. Ma, D. Mao and Y. Huang, In-Situ rolling Friction Stir Welding of Aluminum Alloys Towards Corrosion Resistance, *Corros. Sci.*, 2024, **230**, p 111920.
51. B.J. Kutelu, O.O. Oke and A. Oyetunji, Influence of Welding Speed on Corrosion Susceptibility of 304L Stainless Steel in Chloride Environment, *Int. Multidiscip. Res. J.*, 2023, **4**(5), p 376–380.
52. C. Pandey, M.M. Mahapatra, P. Kumar, F. Daniel and B. Adhithan, Softening Mechanism of P91 Steel Weldments Using Heat Treatments, *Arch. Civ. Mech. Eng.*, 2019, **19**, p 297–310.
53. Z. Fei, Z. Pan, D. Cuiuri, H. Li, W. Huang and Z. Peng, Effect of Post-Weld Heat Treatment on Microstructure and Mechanical Properties of Deep Penetration Autogenous TIG-Welded Dissimilar Joint Between Creep Strength Enhanced Ferritic Steel and Austenitic Stainless Steel, *Int. J. Adv. Manuf. Technol.*, 2020, **108**, p 3207–3229.
54. A. Kellai, A. Lounis, S. Kahla and B. Idir, Effect of Root Pass Filler Metal on Microstructure and Mechanical Properties in the Multi-Pass Welding of Duplex Stainless Steels, *Int. J. Adv. Manuf. Technol.*, 2018, **95**, p 3215–3225.
55. B.N. Güzey and G. İrsel, Investigation of Mechanical and Microstructural Properties in Joining Dissimilar P355GH and Stainless 316L Steels by TIG Welding Process, *Int. J. Press. Ves. Pip.*, 2023, **205**, 104965
56. C. Köse, Dissimilar Laser Beam Welding of AISI 420 Martensitic Stainless Steel to AISI 2205 Duplex Stainless Steel: Effect of Post-Weld Heat Treatment on Microstructure and Mechanical Properties, *J. Mater. Eng. Perform.*, 2021, **10**, p 7417–7448.
57. C. Pandey, N. Saini, M.M. Mahapatra and P. Kumar, Study of the Fracture Surface Morphology of Impact and Tensile Tested Cast and Forged (C&F) Grade 91 Steel at Room Temperature for Different Heat Treatment Regimes, *Eng. Fail. Anal.*, 2017, **71**, p 131–147.
58. M. Khan, M.W. Dewan and M.Z. Sarkar, Effects of Welding Technique, Filler Metal and Post-Weld Heat Treatment on Stainless Steel and Mild Steel Dissimilar Welding Joint, *J. Manuf. Process.*, 2021, **64**, p 1307–1321.
59. A.K. Maurya, A. Bhattacharyya, R. Chhibber and C. Pandey, Structural Integrity and Corrosion Behavior Assessment of the Dissimilar Gas Tungsten Arc Welded Joint of sDSS 2507/IN625 Superalloy, *Mater. Chem. Phys.*, 2024, **318**, 129322
60. H. Wang, K. Wang, W. Wang, L. Huang, P. Peng and H. Yu, Microstructure and Mechanical Properties of Dissimilar Friction Stir Welded Type 304 Austenitic Stainless Steel to Q235 Low Carbon Steel, *Mater. Charact.*, 2019, **155**, p 1–12.
61. A.K. Maurya, S.M. Pandey, R. Chhibber and C. Pandey, Structure–Property Relationships and Corrosion Behavior of Laser-Welded X-70/UNS S32750 Dissimilar Joint, *Arch. Civil. Mech. Eng.*, 2023, **23**(2), p 81.
62. M. Safari, H. Mostaan and E. Derakhshan, Microstructural and Mechanical Studies of the Dissimilar Tabular Joints of Incoloy Alloy 825 and AISI 316 Stainless Steel, *J. Mar. Eng. Technol.*, 2018, **19**, p 176–185.
63. P. Kumar, A.N. Sinha, C.K. Hirwani, M. Murugan, A. Saravanan and A.K. Singh, Effect of Welding Current in TIG Welding 304L Steel on Temperature Distribution, Microstructure and Mechanical Properties, *J. Braz. Soc. Mech. Sci.*, 2021, **43**(7), p 1–20.
64. D. Das, D.K. Pratihari and G.G. Roy, Cooling Rate Predictions and its Correlation with Grain Characteristics During Electron Beam Welding of Stainless Steel, *Int. J. Adv. Manuf. Technol.*, 2018, **97**(5), p 2241–2254.
65. K.Y. Chiu, F.T. Cheng and H.C. Man, Corrosion Behavior of AISI 316L Stainless Steel Surface-Modified with NiTi, *Surf. Coat. Technol.*, 2006, **200**, p 6054–6061.
66. Z. Liu, L. Qiao, R. Cao, H. Dong, C. Wang, H. Che, T. Wang and Y. Yan, A Comparative Study on Microstructure, Mechanical Properties and Corrosion Resistance of m390 and 304 with Different Welding Methods, *J. Mater. Eng. Perform.*, 2023 <https://doi.org/10.1007/s11665-023-08523-y>

Publisher's Note Springer Nature remains neutral with regard to jurisdictional claims in published maps and institutional affiliations.

Springer Nature or its licensor (e.g. a society or other partner) holds exclusive rights to this article under a publishing agreement with the author(s) or other rightsholder(s); author self-archiving of the accepted manuscript version of this article is solely governed by the terms of such publishing agreement and applicable law.